Investigations of Heat Sink Property of a Novel Dual Linear Polarized Low Cross-Polarization X-Band Phased Array Antenna Employing Silicon RFICs-Based Beamforming Network

RUDRAISHWARYA BANERJEE[1] **(Student Member, IEEE),**
SATISH KUMAR SHARMA[1] **(Senior Member, IEEE),**
JIA-CHI SAMUEL CHIEH[2] **(Senior Member, IEEE), AND RAIF FARKOUH**[2]

[1]Department of Electrical and Computer Engineering, San Diego State University, San Diego, CA 92182, USA

[2]Naval Information Warfare Center Pacific, San Diego, CA 92110, USA

CORRESPONDING AUTHOR: S. K. SHARMA (e-mail: ssharma@sdsu.edu)

ABSTRACT In this paper, investigations on heat sink property of a 4x2 wideband dual linear polarized phased array antenna comprised of 3D metal printed all metallic radiators, serving also as heat sink, is presented for X-band frequency. Two single radiators, each with a height nearly equal to $\lambda/2$ corresponding to center frequency (9.50 GHz), shaped intuitively and placed orthogonal to each other and surrounded by a metal ring of square cross-section with overall dimension of $\lambda/2 \times \lambda/2$, constitutes the dual linear polarized radiating element. Both radiators are fed by an orthogonal arrangement of stripline feeds through a trapezium shaped metal plate, which in turn helps to integrate the antenna aperture with the beamforming network (BFN). A set of via fences are placed beneath each antenna element, which work as a thermal path between the BFN and antenna aperture. This radiating element resembles heat fins, and designed to cover 8.5-11.5 GHz impedance bandwidth. Good radiation pattern with low cross-polarization is obtained over the entire bandwidth, while the peak broadside gain is varying between 14-11 dBi. Beam scans are viable $\pm 50°$ in $\varphi = 0^0$ plane and $\pm 30°$ in $\varphi = 90^0$ plane. The array antenna aperture is built using 3D metal printing technology. The BFN is comprised of commercial silicon Radio Frequency Integrated Circuit (RFIC) chips which have been integrated with the antenna aperture. A beamforming algorithm is applied through serial peripheral interface (SPI) controller to achieve beam steering during the measurement process. The temperature reduction of 60°C is achieved with the heat sink structure when the temperature distribution of BFN with and without heat sink are compared for the 4x2 array. The temperature of the heat sink antenna is only 41°C and the temperature distribution is validated with an infrared (IR) camera.

INDEX TERMS Heat sink, 3D metal printed, dual linear polarized, phased array, RFIC, beamforming.

I. INTRODUCTION

NAVAL ships require high-speed wireless communications to improve their image sharing, multimedia data sharing, and accelerate better coordination in battlefield operations. The antennas that support high data rate wireless network require a wide impedance bandwidth, stable radiation patterns, high gain, and beam steering properties.

Electronic scanning phased array antenna radiates huge amount of microwave power in an intended direction, as well as provides instantaneous beam steering [1], [2]. Recently phased array antennas with integrated beamforming networks comprised of silicon RFICs have gained major attention.

The coauthors (Sharma and Chieh) of this paper have earlier published phased arrays using similar RFICs [3]–[5]

at Ku- and Ka- bands using Anokiwave RFICs and have successfully shown beam steering performance. In [5], an 8 × 4 dual linear polarized stacked patch phased array antenna used a RFIC per radiating element and employed as a feed source for a reflector antenna. The temperature measured on the antenna aperture side of the patch array using the infrared (IR) camera is 58.4°C. The measured peak power consumption of this antenna was 6.3W (3.5A, 1.8V). The coplanar waveguide (CPW) transmission lines along with ground via fencing is employed to excite the driven patch, where the ground vias help in impedance matching as well as in heat spreading.

With the recent advancement of the commercial silicon beamforming chipsets, the heat generated by the chips in the beamforming network (BFN) attached with the antenna aperture can become a problem, and hence cooling arrangement should be included to solve this. Again, heat sinks are made of metal materials, and if heat sink dimensions are comparable to the wavelength at operating frequency, it can cause unwanted electromagnetic interference [6]–[8]. As radiation from heatsinks is usually undesirable, bonding posts are employed to ground the heatsink structure to a nearby printed circuit board (PCB) to mitigate heatsink radiation in [9] and [10].

An antenna structure that can serve as radiator as well as heat sink, can be proposed as a solution for the phased array antennas that employ RFICs based BFN. A radiator working as heat sink as well, was proposed in [11], where a heat sink loaded patch with improved radiation efficiency was explored. In [12], a 3-D fractal heatsink antenna is proposed, with improved radiation efficiency and gain and lower thermal resistance in comparison to a conventional fin shaped heat sinks. However, these proposed configurations consist of a single antenna working at low frequencies.

One important aspect for the heat sink antenna is the choice and placement of thermal spreader between the heat source and heatsink. The metallic thermal via is a widely used structure as in [13] and [14]. In [13], a single polarized stepped notch antenna attached to a flat multi-layered printed circuit board (PCB), working at Ku-band, is proposed which, along with serving as a radiator, provide a thermal heat sink for active arrays as well. The heat generated by the active devices, such as high power amplifiers (HPA) or low noise amplifiers, passes through the PCB, into the antenna aperture through plated holes which provide the principal heat path. A thin radome is placed above the 26 x 11 notch array, and a maximum temperature of 60°C is noted with 40° C inlet air flow of 0.425 m³/s, and a heat load of 50 W. In [14], a single polarized 4x4 heat sink antenna array on low-temperature cofired ceramic (LTCC) substrate is proposed, where the antenna element is a horn-like structure that consists of an open-ended waveguide and two vertical metallic fins, and the feeding network is comprised of the substrate integrated waveguides (SIWs) with numerous metallic vias, which in turn, helps to transfer the heat from chips to the heatsink, and temperature reduction of 40.1°C is achieved.
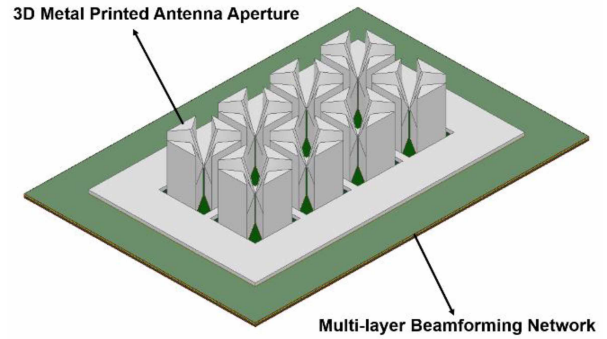

FIGURE 1. All metal 3D metal printed dual linear polarized 4x2 phased array heat sink antenna with integrated beamforming.

In [15], preliminary study on a 4 ×8 dual linear polarized phased array antenna, comprised of all metallic radiators, serving also as heat sink as well, is presented for Ku-band wireless communication applications. In this paper, a 4x2 dual linear polarized phased array antenna, as shown in Fig. 1, with all metal 3D printed radiating elements, is thoroughly investigated for heat sink property. Considering the fact that we will be using X-band Anokiwave chips (AWMF-0101) for the beamforming network, the radiator is designed to cover 8.5-11.5 GHz and shaped intuitively in such a way that the antenna array aperture can serve as a heat sink as well. A design principle of this new wideband metallic radiator is provided in the following sections. The antenna aperture is integrated with a multilayered BFN employing Anokiwave RFICs. The scanning performance and thermal analysis of the structure is presented here which is discussed in the later sections. Section II of this paper describes the configuration and heat sink properties of the single polarized antenna. Section III includes the discussion about the dual polarized antenna structure, the stack-up description of the BFN, and presents a design guideline for the proposed radiator. Section IV describes the design of the 2x2 subarray along with thermal analysis of the 2x2 dual polarized sub-array. Section V presents the 4x2 array structure and performances along with heat sink study of the 4x2 array. Section VI presents the discussion about the chip and BFN, and the fabrication and measurement results. Section VII discusses the conclusion.

II. NOVEL RADIATING ELEMENT WITH HEAT SINK FEATURE
A. STUDY OF THE STANDALONE RADIATING ELEMENT
Initially, a two-armed unique radiator surrounded by a metal ring, is intuitively designed for X-band applications in such a way that it will be working as a heat sink as well as a wideband radiator. The top view and side view of the proposed standalone radiator is shown in Figs. 2(a) and 2(b) with specified dimensions where λ corresponds to the center frequency (9.50 GHz). The standalone radiator is fed by a lumped port. The radiator has two parts: two shaped flared vertical arms and one metal ring around the two arms.
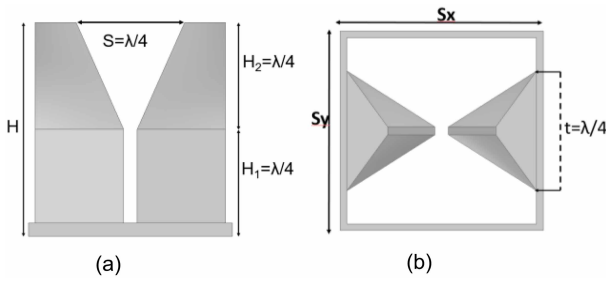
FIGURE 2. The single polarized standalone antenna (a) side view, and (b) top view.

FIGURE 4. Peak gain versus frequency for the single polarized standalone radiator for different heights.
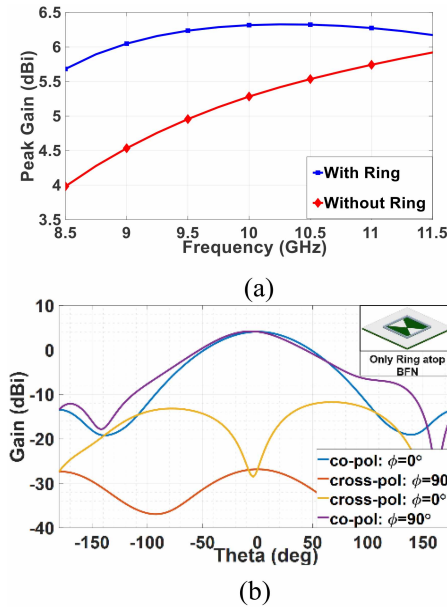

FIGURE 3. (a) Peak gain versus frequency for the single polarized standalone radiator with and without metal ring, and (b) Radiation pattern of the only metal ring atop BFN at 9.50 GHz (without two-armed radiator).
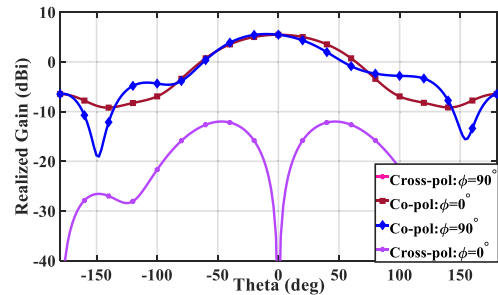
FIGURE 5. Radiation pattern of the single polarized standalone radiator at 9.50 GHz.

The two armed structure is combined with the outer metal ring which in turn radiates like a rectangular large loop antenna of $\lambda/2$ x $\lambda/2$ cross-section, thereby improving the gain of the antenna. This metal ring helps in the fabrication of the array aperture and its integration with the beamforming board in addition to improving radiation performance. The peak accepted gain versus frequency for a radiator with and without metal ring is shown in Fig. 3(a). From Fig. 3(a), it is clear that the proposed radiator is wideband subject to impedance matching can be achieved. Also, we can see that the peak accepted gain improves by approximately 1.5 dB towards the lower end and to approximately 1 dB towards the higher end of the bandwidth when the ring is employed. To further clarify the contribution of the ring, the radiation pattern of the only rectangular ring (without the two-armed structure) atop BFN stack up (described in Section III) at 9.50 GHz is shown in Fig. 3(b), which shows that the ring is radiating in broadside direction. Here the ring is not fed like a conventional loop antenna and therefore, it is not properly matched for the operating band. However it is getting induced excitation through the trapezium shaped metal plate
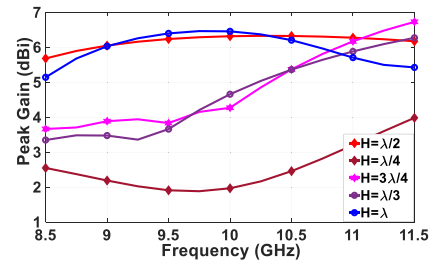
(shown later in Fig. 8(b)) where the two-armed radiating element is attached with BFN, hence it works as an inefficient loop radiator.

The radiator is designed with a target to cover 8.5-11.5 GHz impedance bandwidth which includes the bandwidth offered by RFICs employed for the BFN. The radiator dimensions are optimized for X-band through thorough parametric study. It is clear from the peak gain versus frequency curves in Fig. 4 that the overall radiator height, $H = H_1 + H_2$, should be $\lambda/2$ corresponding to 9.50 GHz to get the best performance. After a thorough parametric study, it is observed that optimum combination of the flared and non-flared heights of the radiator is $H_1 = H_2 = 8$ mm, whereas the width is $t = 8$mm and flare of the radiator, $S = 8$mm, which is $\lambda/4$ at 9.50 GHz. The radiator is surrounded by a square metal ring of overall dimensions $\lambda/2 \times \lambda/2$ corresponding to 9.50 GHz. The radiation pattern of the single polarized radiator at 9.50 GHz is shown in Fig. 5. The radiation pattern shows a peak realized gain of 5.4 dBi, in addition to the co- to cross-polarization separation of 17 dB.

B. HEAT SINK PROPERTY OF THE RADIATING ELEMENT
We have employed Ansys Icepak for the heat sink study. Ansys Icepak is based on Navier-Stoke's equations [16]. Navier-Stoke's equations of fluid mechanics involves partial differential equation that describes the flow of incompressible fluids. Ansys Icepak solves the Navier-Stokes equations for transport of mass, momentum, and energy. The governing equations for Ansys Icepak are as follows [16].

(i) The Mass Conservation Equation:

$$\frac{\partial \rho}{\partial t} + \nabla.(\rho.\overrightarrow{v}) = 0. \tag{1}$$

(ii) Momentum Equation:

$$\frac{\partial \left(\rho \overrightarrow{v} \right)}{\partial t} + \nabla.\left(\rho.\overrightarrow{v}\,\overrightarrow{v} \right) = -\nabla p + \nabla.(\overline{\tau}) + p\overrightarrow{g} + \overrightarrow{F} \tag{2}$$

where, stress tensor is given by,

$$\overline{\tau} = \mu \left[\left(\nabla \overrightarrow{v} + \nabla \overrightarrow{v}^T \right) - \frac{2}{3} \nabla.\overrightarrow{v}.I \right] \tag{3}$$

Here, p is the static pressure, $p\overrightarrow{g}$ is the gravitational body force, and $\overrightarrow{F}$ contains other source terms. And μ is the molecular viscosity, I is the unit tensor, and the second term on the right-hand side is the consequence of volume dilation.

(iii) Energy Conservation:

$$\frac{\partial}{\partial t}(\rho h) + \nabla.\left(\rho h \overrightarrow{v} \right) = \nabla.[(k + k_t)\nabla T] + S_h \tag{4}$$

where, sensible enthalpy is given by

$$h = \int_{T_{ref}}^{T} c_P dT \tag{5}$$

where, T is the temperature, T_{ref} is 298.15°K and ρ is the density. Here, k is the molecular conductivity and k_t is the conductivity due to turbulent transport.

$$k_t = c_p \mu_t / Pr_t \tag{6}$$

The source term S_h takes into account any volumetric heat sources defined by the user.

$$\frac{\partial}{\partial t}(\rho h) = \nabla.(k\nabla T) + S_h \tag{7}$$

A conduction equation, that contains the heat flux due to conduction and volumetric heat sources within the solid, is solved by Icepak in conducting solid regions.

The Anokiwave RFIC (AWMF-0101) employed in our BFN design has measured peak power consumption of 1.35 Watts which is dissipated as heat. Each chip feeds four dual polarized radiating elements simultaneously. Thus, each 2x2 subarray is fed by one RFIC source which in turn shares heat dissipation resulting from the measured peak power consumption of 1.35 Watts. The radiators are realized using the 3D metal printed process and hence we considered solid aluminum alloy (*AlSi10Mg*, conductivity 600000 S/m) for all the radiating element simulations. For thermal analysis, no forced air flow or no forced cooling arrangement is considered, and there is opening all around the antenna with air at room temperature, i.e., 26.85°C (300°K) and a velocity of 0.1m/sec against gravity (indoor air flow can be assumed as 0.1m/sec).

Before describing thermal analysis of the proposed 2x2 subarray, we present the thermal analysis of the BFN stack-up of this subarray (Fig. 6) without the proposed antenna structure atop it, assuming the chip at center below BFN has power consumption of 1.35 Watts. We noted that
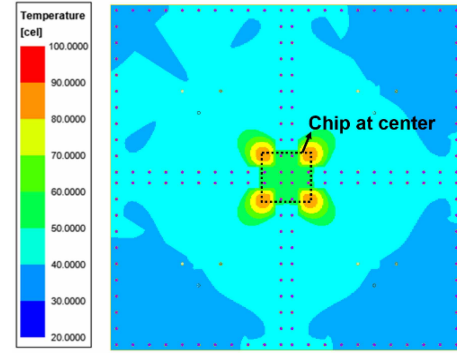

FIGURE 6. Temperature distribution of the BFN stack-up without antenna aperture (heat sink) with a RFIC of measured peak power consumption of 1.35 Watts below it.

the maximum temperature, without heat sink, ranges up to 90°C. Here, it should be noted that the temperature distribution has four peaks at four corners of the chip, whereas temperature at the center position of the chip is lower than the maximum temperature. This is due to the presence of metal vias at the center of the stack up (as shown in Fig. 6) which work as thermal spreaders.

Now, a single polarized 2x2 subarray antenna atop BFN is simulated with the same 1.35 Watts at the center below the BFN stack-up. We can notice, in the 2x2 subarray, each radiator is connected with the adjacent radiator, thereby creating a continuous metal structure. This helps in realizing the array antenna aperture using 3D metal printing in addition to improved heat sink property. Fig. 7(a) shows the top view of the antenna and the isometric view is shown in Fig. 7(b). We can observe that the temperature varies between 39-42°C which is evenly distributed across the antenna aperture. If we compare this with the temperature distribution of the BFN without heat sink, we can observe that the proposed heat sink antenna aperture helps to reduce the temperature by approximately 50°C compared to a structure without the heat sink. Fig. 7(c) shows the temperature distribution of the bottom view, where we observe that the maximum temperature is 60°C. The reduction in temperature happens because of the periodic arrangement of conducting copper vias underneath each radiator (shown in Fig. 8) helps in spreading the heat from the source at the bottom surface of the PCB to the antenna atop BFN, and the heat sink antenna in turn further reduces temperature by spreading out the heat to the surrounding air. Heat sink employs the principle of thermal diffusion and air convection, where heat sink continuously diffuses heat in surrounding air and the heated air become lighter and moves upward and reduced temperature is maintained in this way.

In view of the above, while designing the proposed heat sink antenna structure, the target is to maximize the surface area of the structure to enhance the interaction of the structure with air, whereas the thermal spreaders transport the heat from the chips to the heat sink and distribute the heat over entire structure evenly. On the other hand, our aim is to
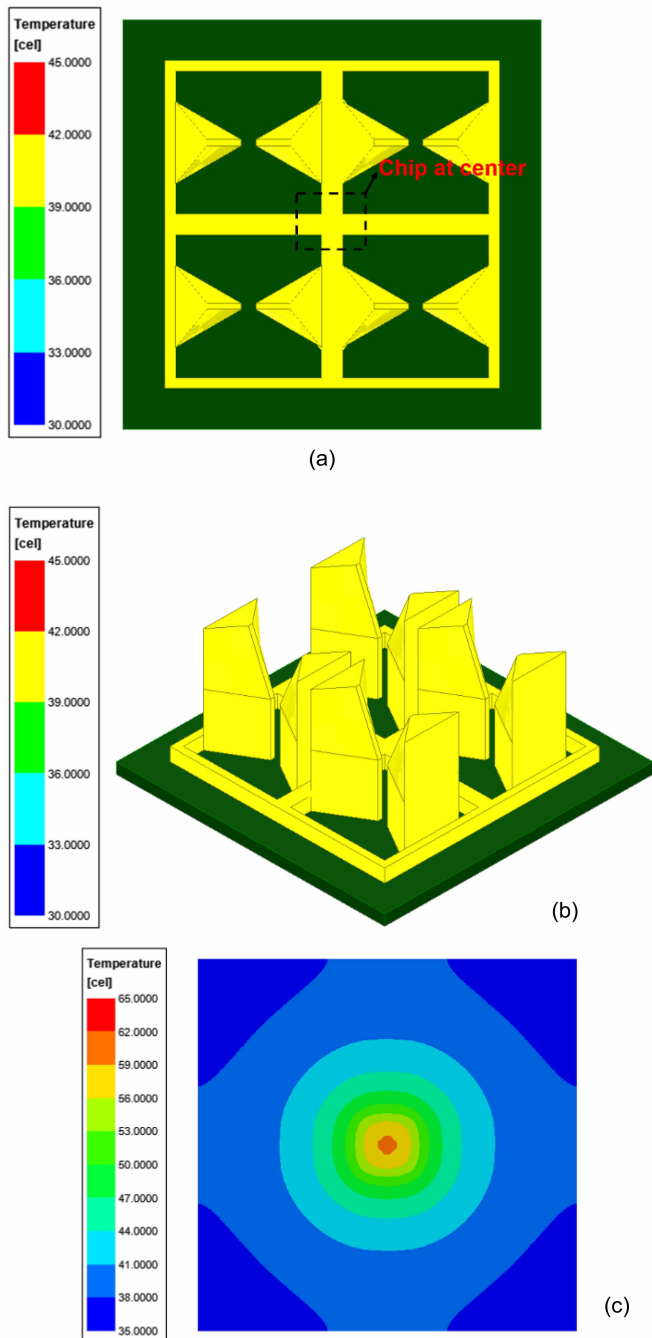
FIGURE 7. Temperature distribution of 2x2 all metal heat sink antenna atop a RFIC with the peak power consumption of 1.35 Watts (a) top view, (b) isometric view, and (c) bottom view.

design a dual linear polarized antenna array. Hence in this case, we have to take into account the heat sink performance as well as the coupling between the X- and Y-polarized radiators. In the next section, we discuss additional details about this aspect of the design and analysis.

III. DUAL LINEAR POLARIZED RADIATING ELEMENT
A. STACK-UP DESCRIPTION OF THE PCB
As mentioned earlier, while discussing Fig. 7, Fig. 8(a) shows the PCB stack up and feed structure used for the array

implementation. Rogers 4350B ($\varepsilon_r = 3.48$ and $tan\ \delta = 0.004$) is used throughout the board as a core material. The total thickness of the PCB is approximately 45 mils. Two sets of blind vias are used in this design to route RF signal to the dual polarized element. A set of blind vias are present underneath each metal ring for shorting the ground planes. These blind vias in turn helps in suppressing the surface waves generated due to multi-layered substrate as well as helps in heat transfer.

The thermal expansion coefficient of RO4350B material is comparable to that of copper [17]. The coefficient of thermal expansion (CTE) of copper is 16 ppm/°C, whereas that for R4350B is 10 ppm/°C along X-axis and 12 ppm/°C along Y-axis. So the material shows excellent dimensional stability which makes it good for mixed dielectric multi-layer boards construction. The PCB has eleven metal layers, with different power, ground, and digital routing planes underneath the stripline feed layer to bias and control the Anokiwave chipsets. Two orthogonal striplines (Fig. 8(a)), employed to feed two orthogonal two-armed antenna structures, are perpendicular to each other and placed asymmetrically between the two same ground planes, which provides dual-linear polarization as discussed in the next subsection. The power splitter network that feed the chips is simulated in Ansys HFSS and the BFN layout is developed in Altium software. There is a square shaped copper ring with trapezium shaped plates of the same dimension as antenna footprint with an adhesive layer of bulk conductivity of 263160 S/m atop it on the top surface of the stack-up as shown in Fig. 8(b). This conducting adhesive helps to adhere the antenna aperture with the BFN. The exploded bottom view and top view of the antenna and BFN stack-up are shown in Fig. 8(c) and Fig. 8(d), which explains arrangement of the stripline, microstrip line and vias underneath each metal ring around the two orthogonal two-armed antenna structures.

B. DUAL LINEAR POLARIZED SINGLE ELEMENT ATOP PCB STACK-UP
In the dual polarized radiating element another two-armed flared structure is placed perpendicular to the first one within the same metal ring. The single polarized radiator is a two-armed balanced radiator, and hence, balanced feed technique should be applied. Here stripline1 and stripline2 are employed to feed Y-polarized and X-polarized radiators, respectively. These striplines are placed perpendicular to each other, on both sides of a prepeg layer, and are placed asymmetrically between ground planes 3 and 4, as shown in Figs. 8(a) and 8(b). The Figs. 8(e) and 8(f) show the isometric and top view of the structure of the dual polarized single radiating element, respectively.

It is observed from the gain versus frequency graph (Fig. 4) of the single polarized radiator that the best performance is obtained when overall height of the radiator is $\lambda/2$ corresponding to 9.50 GHz. Fig. 9(a) shows the parametric study for the magnitude of reflection coefficient for X-polarized radiator for different combinations
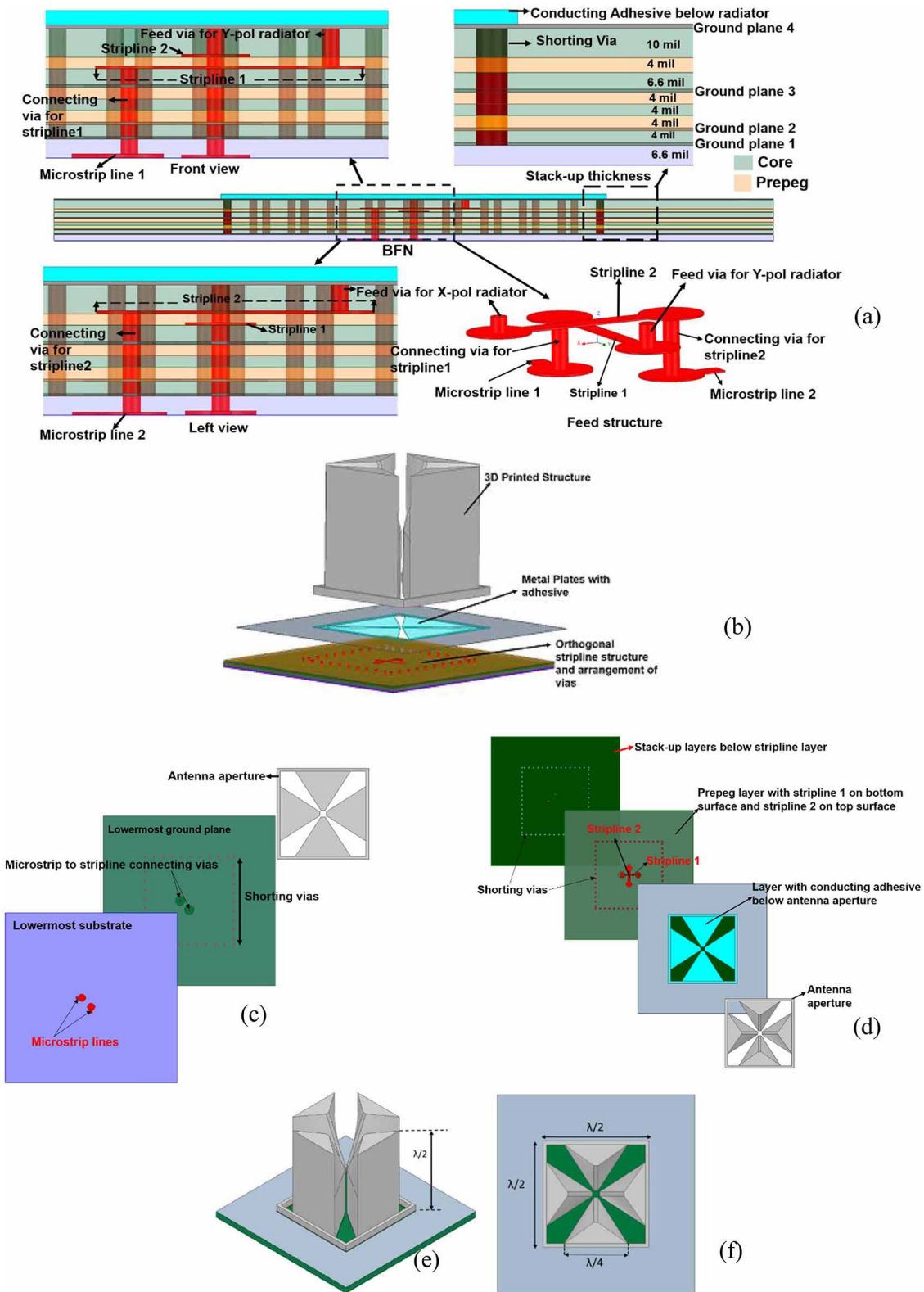
FIGURE 8. (a) Side view of the PCB stack up of the multi-layered feed structure with zoomed in feed structure, (b) Exploded isometric view of the antenna structure and feed structure, (c) Exploded bottom view of the stack-up and antenna aperture, (d) Exploded top view of the stack-up and antenna aperture, (e) Isometric view of the antenna structure and (f) Top view of the antenna structure.

of H_1 and H_2. It is observed that optimum bandwidth is obtained for $H_1 = H_2 = \lambda/4$ corresponding to 9.50 GHz. Fig. 9(b) shows the parametric study for the magnitude of

reflection coefficient for X-polarized radiator for different values of the thickness, t of each arm of the radiator. It is observed that optimum bandwidth is obtained for $t = \lambda/4$
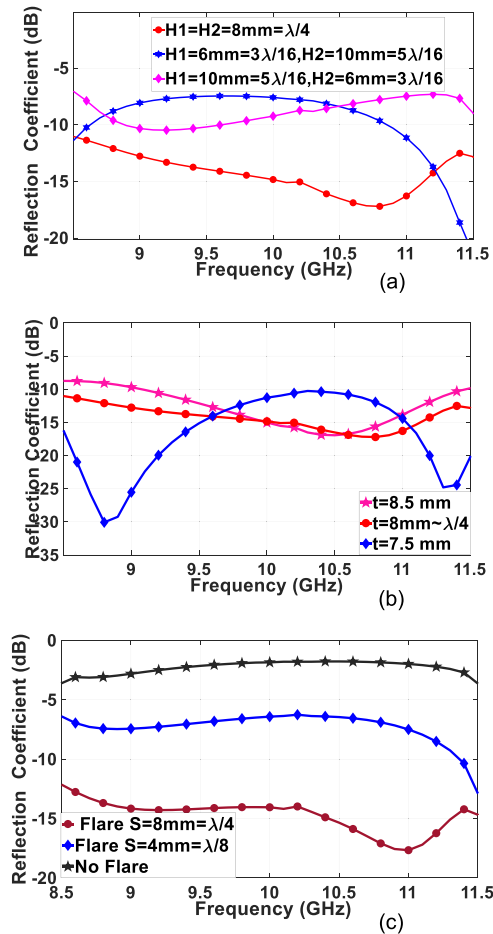
FIGURE 9. The magnitude of reflection coefficient for (a) different combinations of H_1 and H_2, (b) different values of 't', and (c) different flare value 'S' for X-polarized array.

corresponding to 9.50 GHz. Fig. 9(c) shows the parametric study for the magnitude of reflection coefficient for X-polarized radiator for different flare values 'S' of the radiators. Satisfactory impedance matching is obtained for $S = \lambda/4$ corresponding to 9.50 GHz. Identical performances are observed for the Y-polarized radiator, hence not shown for the sake of brevity.

Fig. 10(a) shows the magnitude of reflection coefficient for both polarizations and isolation between two ports and Figs. 10(b) and 10(c) show the radiation patterns at 9.50 GHz for X- and Y-polarized radiators for the optimum dimensions. It can be observed that the single dual-polarized element provides wideband performance with respect to S_{11} of -10dB between $8 - 11.5$ GHz and port to port isolation (S_{21}) of around -20 dB, along with acceptable radiation pattern. But the separation between peak co- and cross-polarized fields is not more than 15dB, which may become worse for the array implementation. This non satisfactory co-cross separation is resolved in the next section while designing the 4x2 array.

Brief design guidelines for this wideband dual linear polarized radiator can be developed from the above observations.
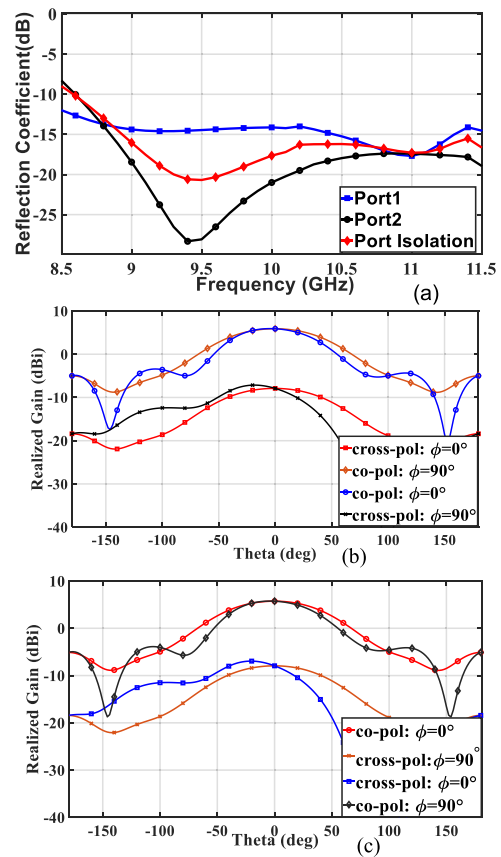

FIGURE 10. (a) The magnitude of reflection coefficient for both polarizations and isolation between the two ports, and Radiation patterns at 9.50 GHz for (b) X-polarized radiator, and (c) Y-polarized radiator.
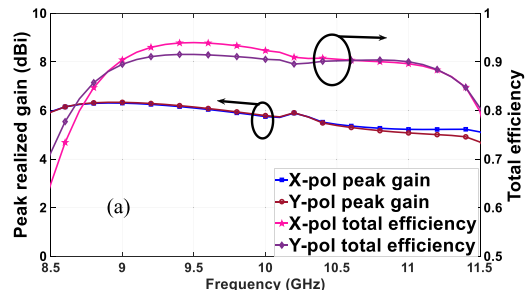

FIGURE 11. Peak gain versus frequency and Total efficiency versus frequency for both X-polarized and Y-polarized radiators.

1. The height of each arm of the radiator is nearly $H = \lambda/2$ at the center frequency
2. The height of the flared and non-flared sections should be $(H1 + H2) = (\lambda/4 + \lambda/4) = \lambda/2$
3. The thickness (t) of each arm is nearly $\lambda/4$
4. The width of the flare should be $S = \lambda/4$
5. The dimension of the metal ring is $Sx = Sy = \lambda/2$

The peak realized gain and total efficiency (Factoring mismatch and dielectric and Ohmic losses) for the both X- and Y-polarizations is shown in Fig. 11. Peak realized gain varies from $5 - 6$ dBi for both polarizations, whereas the efficiency
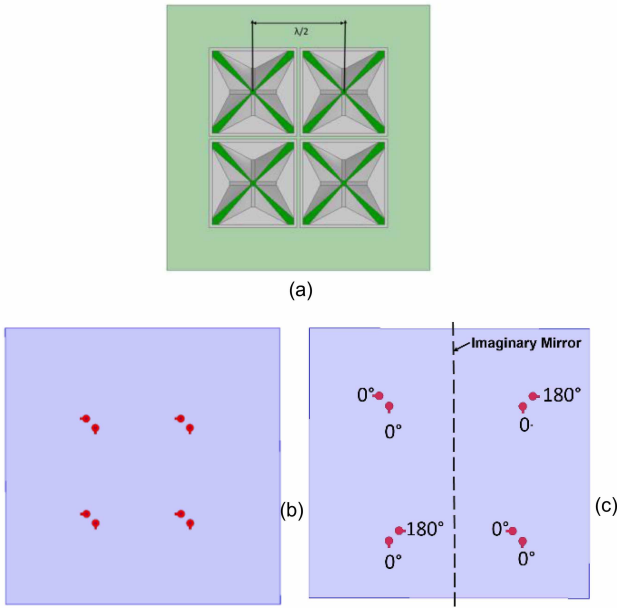
FIGURE 12. Top view of a 2x2 all metal heat sink array (same for configurations I, and II), (b) Bottom view of configurations I, and (c) Bottom view of mirror feed configurations II showing feed orientations and phase values.
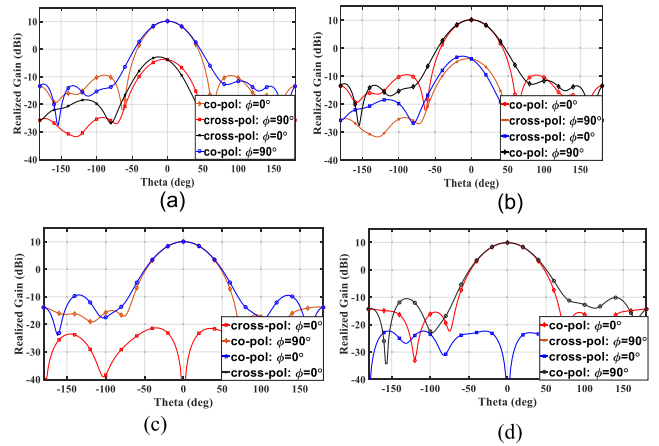

FIGURE 13. Radiation Patterns at 9.5 GHz, (a) X-polarized array for Configuration I, (b) Y-polarized array for Configuration I, (c) X-polarized array for Configuration II, and (d) Y-polarized array for Configuration II.

is above 85% over the entire bandwidth. Considering the 3D metal printing using the aluminum alloy, the total efficiency is quite good.

IV. 2X2 SUBARRAY USING DUAL POLARIZED ELEMENT
A. 2X2 SUBARRAY CONFIGURATION
The top view of a 2x2 all metal heat sink subarray is shown in Fig. 12(a). Here, the inter-element spacing is half of the free space wavelength (λ/2) corresponding to 9.50 GHz, i.e., 16mm. In Figs. 10(b) and 10(c), it is observed that the peak cross-polarization level is quite high. With an aim to reduce peak cross-polarization level, two different feed configurations of 2x2 subarray are studied. Bottom view of the configurations I, and II are shown in Figs. 12(b), and 12(c), respectively. Configuration I employs the conventional feed structure of a 2x2 subarray. In configuration II, the upper right and the lower left elements are mirrored with respect to a vertical plane [18]. The mirror ports must be excited with a 180° phase to achieve in phase or broadside radiation, as shown in Fig. 12(c). The radiation pattern for both polarizations of configuration I are shown in Figs. 13(a) and 13(b) and configuration II are shown in Figs. 13(c) and 13(d), respectively. We can observe that configuration II causes notable cross-polarization improvement as compared to conventional array, which makes it a better choice for the bigger array. Configuration II provide more than 30dB co- to cross-polarization separation whereas only 15 dB separation is obtained for the conventional array.

B. HEAT SINK PROPERTIES
Figs. 14(a) and 14(b) show the top view and isometric view of the thermal analysis (Simulation setup as in single polarized 2x2 subarray)) of a dual polarized 2x2 subarray assuming a RFIC of 1.35 Watts of power consumption at center dissipating as heat. It is observed that the temperature ranges from 36-39°C. Fig. 13(c) shows the bottom view of the array where we can see the maximum temperature is nearly 59°C which is similar to Fig. 7(c) with the same source.

In heat sink study, usually cooling fluid passes across the surface of the warm heat sink and heat sink diffuses the heat in air. So if we assume air flow in one particular direction over heat sink, we observe the temperature of the outlet air is much higher than the inlet air. Here, we have assumed that the whole antenna is in air box with a velocity of 0.1m/sec against gravity (indoor air flow). Although dual polarized antenna offers more metal surface area to diffuse more heat, the dual polarized structure is offering hindrance in normal air flow due to the presence of antenna elements in both X- and Y-directions, therefore, we have observed little difference in the temperature distribution between the single polarized (39-42°C) and dual polarized (36-39°C) sub-arrays.

V. 4X2 ANTENNA ARRAY CONFIGURATION
A. THE 4X2 DUAL POLARIZED ARRAY WITH MIRROR FEED STRUCTURE
The 4x2 dual polarized array is designed using the subarray discussed in Figs. 12(a) and 12(c) with mirror configuration. The array has overall dimension of 104 mm x 84 mm, with 8 radiating elements and total 16 ports. Fig. 15 shows the top view of the 4x2 antenna aperture. Here, the inter-element spacing is designated as $Dx = Dy = 16$ mm (λ/2 at 9.50 GHz), and width $W1 = 2 \times 16 = 32$ mm, Length $L1 = 4 \times 16 = 64$ mm, $W2 = 52$ mm, $W3 = 72$ mm, $L2 = 84$ mm, $L3 = 104$ mm. It is to be noted that each single element structure is connected with the adjacent structure. Also, there is metal extension around the 4x2 radiating aperture, which in turn helps in 3D metal fabrication of a
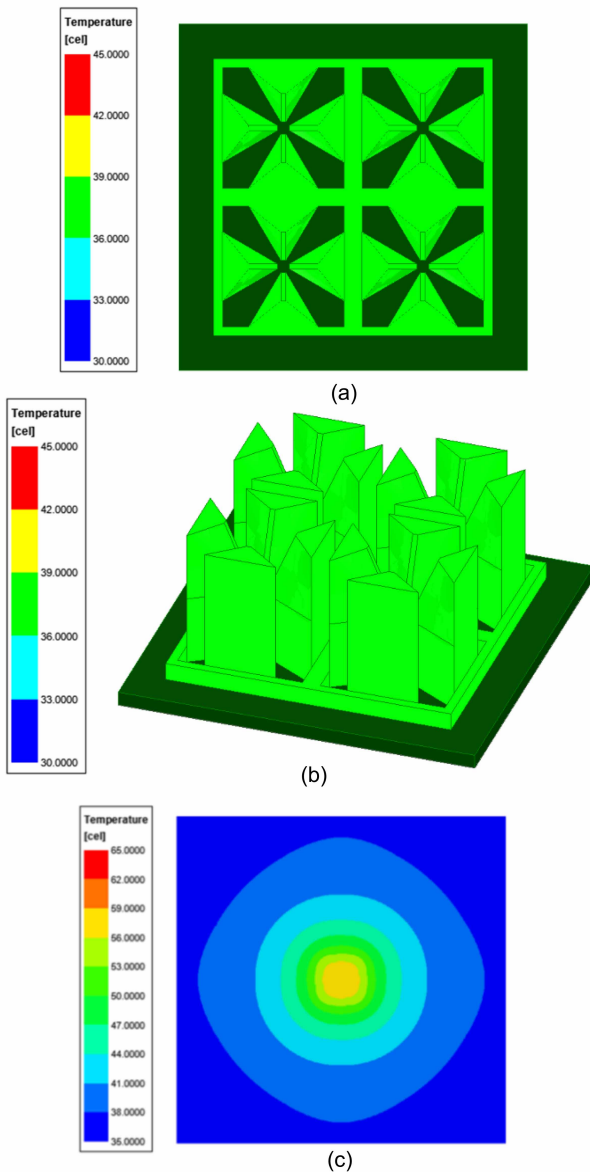
FIGURE 14. Temperature distribution of 2x2 dual polarized antenna aperture atop a RFIC of power consumption of 1.35 Watts (a) Top view, (b) Isometric view, and (c) Bottom view.
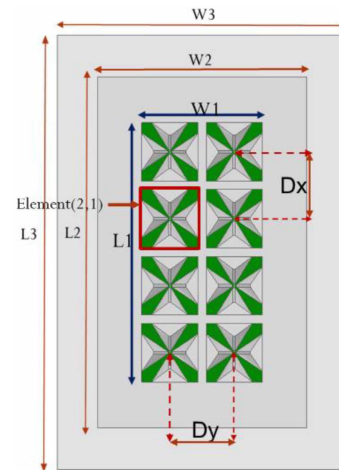

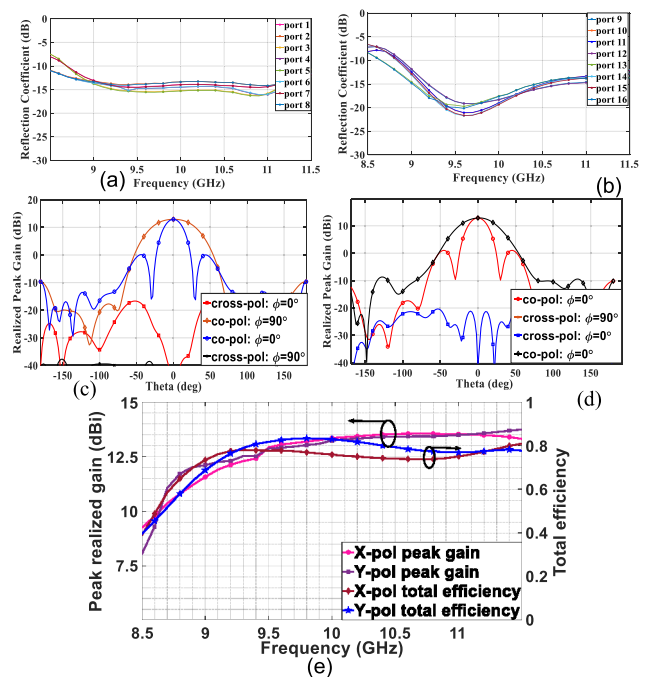FIGURE 15. Top view of the 4x2 all metal heat sink antenna array.

FIGURE 16. (a) The magnitude of reflection coefficient for X-polarized array for all ports, (b) The magnitude of reflection coefficient for Y-polarized array for all ports, (c) Radiation pattern at 9.5 GHz for X-polarized array, (d) Radiation pattern at 9.5 GHz for Y-polarized array, and (e) Broadside peak realized gain and total efficiency for both polarizations.

continuous metallic antenna aperture, and in addition helps in enhancing the heat sinking property.

Magnitude of the reflection coefficients for all the ports for X- and Y-polarized array elements are shown in Figs. 16(a) and 16(b), respectively. The broadside radiation pattern of the X-polarized array and Y-polarized array at 9.50 GHz are shown in Figs. 16(c) and 16(d), respectively. It is observed that the array offers good impedance matching over 8.5-11.5 GHz with excellent broadside radiation pattern, the peak co- to cross-polarization separation being more than 20 dB over entire bandwidth. Fig. 16(e) shows the peak realized gain and the total efficiency. We can observe that the total efficiency is nearly 80% which is acceptable considering that we are using aluminium alloy with a conductivity of

600000S/m. The peak realized gain varies between 11 dBi to 14 dBi over the entire bandwidth.

Figs. 17(a) and 17(b) show the scanning performance of both X-polarized and Y-polarized cases in $\varphi = 0^0$ plane. In Fig. 17(a) and 17(b), it can be seen that gain drops from 12.8 dBi to 12.5 dBi as beam scans till $\pm 50°$ for X-polarized case and $\pm 45°$ for Y-polarized case in $\varphi = 0^0$ plane. Figs. 17(c) and 17(d) show the active S-parameter of the Element (2, 1) for the broadside and $\pm 50°$ beam scan in $\varphi = 0^0$ plane for the both X-polarized and Y-polarized cases. It is observed that active S-parameter is below -10dB almost over entire bandwidth for maximum scan as well.
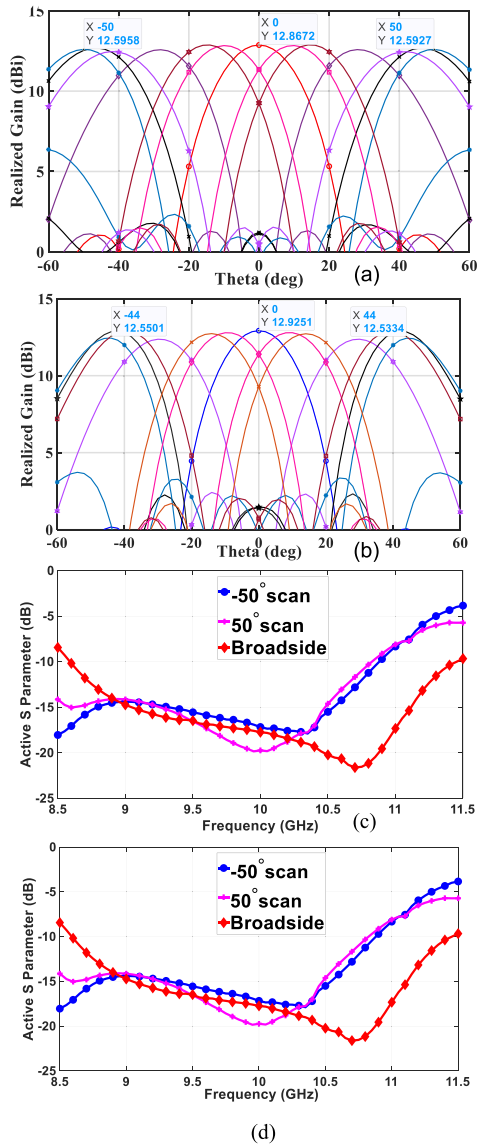
FIGURE 18. Temperature distribution of the BFN without the 4x2 heat sink radiator antenna with the two chips where each chip has power consumption of 1.35 Watts.

FIGURE 17. Scanning performance of the 4x2 array in $\varphi = 0^0$ plane for (a) X-polarized array, and (b) Y-polarized array. Active S-parameter for the broadside and maximum scan angle for (c) Element (2, 1) for X-polarized radiator, and (d) Element (2, 1) for Y-polarized radiator.

FIGURE 19. Temperature distribution of 4x2 array antenna with the two chips each having power consumption of 1.35 Watts: (a) isometric view, (b) top view, and (c) bottom view.

B. THERMAL ANALYSIS OF THE 4X2 DUAL POLARIZED ARRAY

For thermal analysis included here, there is no forced air flow or no forced cooling arrangement. One Anokiwave X-band chip is feeding four dual polarized radiators, as discussed earlier. Each chip has a RF power consumption of 1.35 Watts which dissipates as heat. Here, two chips are present underneath the 4x2 antenna array aperture. There is opening all around the aperture with air at room temperature, i.e., 26.85°C (300°K) with a velocity of 0.1m/sec against gravity.

The temperature distribution of the BFN without the heat sink (antenna aperture) is shown in Fig. 18. It shows that the maximum temperature of the BFN is approximately 100°C
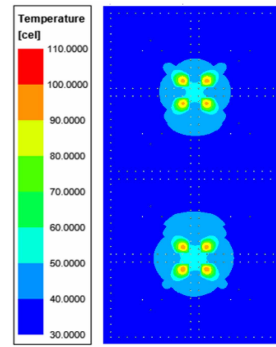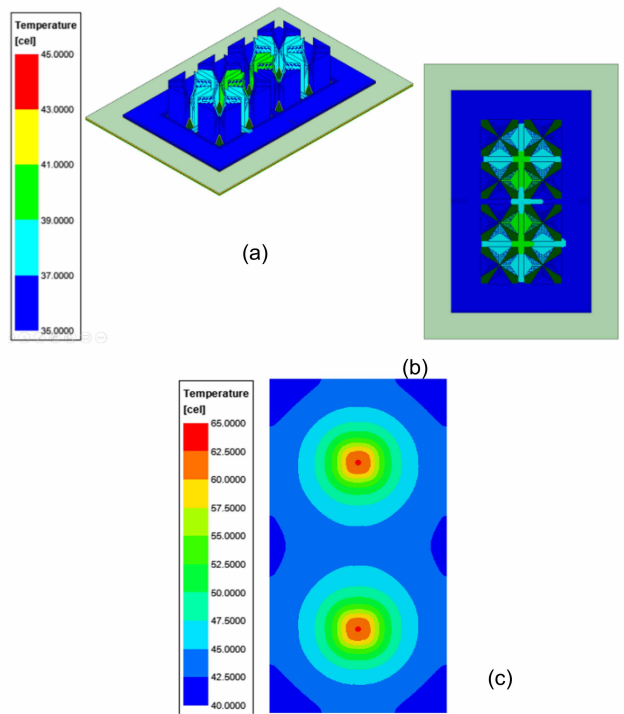
without the heat sink structure. Here also we can notice the peak of temperature distribution is located at the positions of four corners of the chip (as observed in Fig. 6 as well).

The results for thermal analysis of the antenna aperture atop BFN is shown in Fig. 19. From Figs. 19(a) and 19(b), we see the maximum temperature of the antenna aperture ranges from 40°-41° C. Since we know that each chip feeds four radiators simultaneously, and located at the center of each 2x2 sub array, which implies two chips are separated by 32mm and each chip individually dissipates 1.35 Watts of the consumed power into heat. Therefore, the overall combined temperature of the backside of the PCB ranges from 40°C to 62°C, as shown in Fig. 20(c). So we can see there is more

FIGURE 21. Temperature distribution of 4x2 array for (a) Aluminum based structure, and (b) Copper based structure.
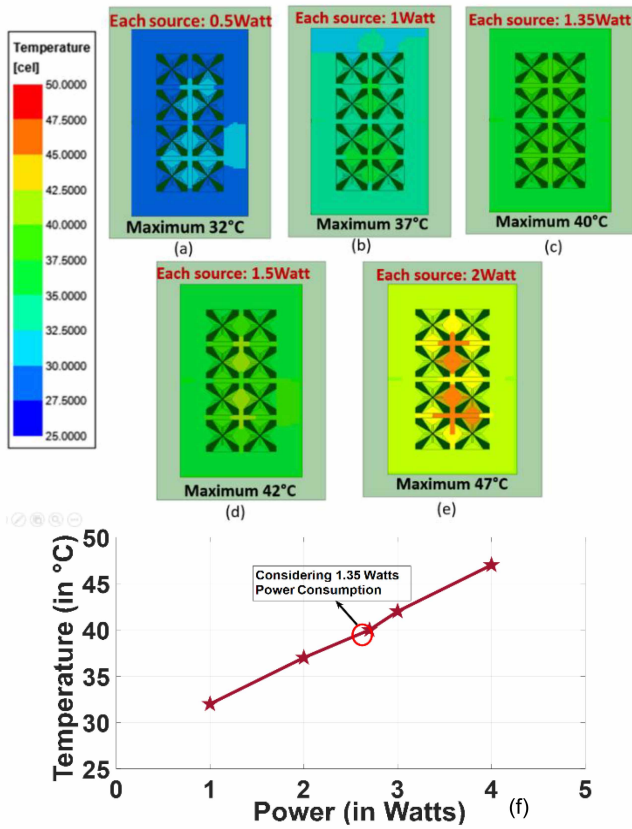

FIGURE 20. Temperature distribution of 4x2 array for the different input power consumptions (a) total 1 Watt, (b) total 2 Watt, (c) total 2.7 Watt, (d) total 3 Watt, (e) total 4 Watt and (f) Input Power versus maximum temperature (the temperature when each chip has power consumption of 1.35 Watts is marked with a box in graph).

FIGURE 22. Temperature distribution of the 4x2 array of aluminium alloy for (a) no air flow, and (b) 0.5 m^3/sec air flow.

than 20°C temperature difference between the temperature of the heatsink and the backside of the BFN board.

With the same simulation setup, the temperature of same antenna structure with different input power is studied, which is shown in Figs. 20(a-e). The input power versus maximum temperature curve is shown in Fig. 20(f), where it is observed that temperature rise is not perfectly linear with the input power, however the rise in power by 1 Watt causes approximately 4-5 °C rise in temperature for the same heat sink structure. It can be noted that when each chip is assumed to be causing power consumptions of 0.5 Watt (total 1 Watt), 1 Watt (total 2 Watt), 1.35 Watt (total 2.7 Watt), 1.5 Watt (total 3 Watt) and 2 Watt (total 4 Watt), the temperature ranges from 27°–32°C, 25°–37°C, 35°–40°C, 35°–42°C and 39°–47°C, respectively.

Figs. 21(a) and 21(b) shows the comparison of the 4x2 antenna aperture simulated with the same simulation setup assuming each chip with power consumption of 1.35 Watts dissipating as heat, where Fig. 21(a) is considering aluminum alloy (already used for other simulations) and Fig. 21(b) is considering copper as material. Since copper is much better heat conductor than aluminum alloy, therefore, we see that temperature ranges from 25°–31° C for copper (Fig. 21(b)) whereas it ranges from 36°–42° C for aluminum
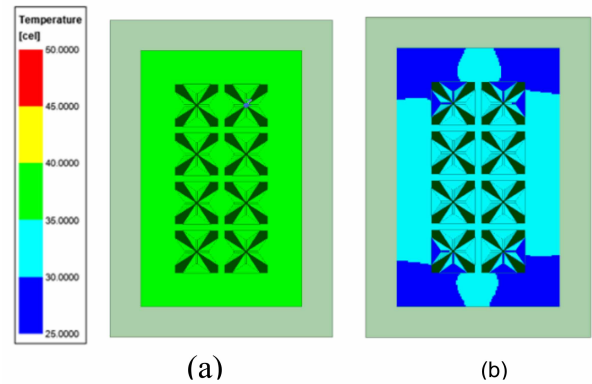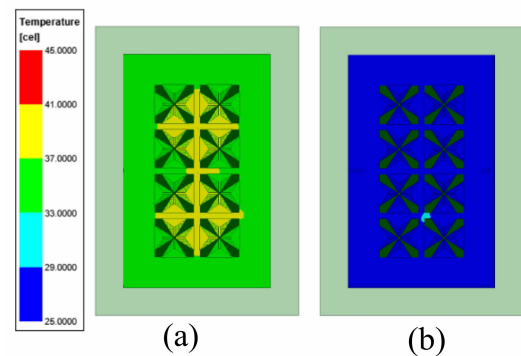
alloy (Fig. 21(a)). So if the same heat sink antenna structure with same dimensions can be built using copper, further temperature reduction of 11°C can be achieved.

Finally, in Figs. 22(a) and 22(b), the comparison of the 4x2 antenna aperture is simulated with same simulation setup assuming each chip has power consumption of 1.35 Watts dissipating as heat, where no air flow is considered in Fig. 22(a) and 0.5 m^3/sec air flow is considered for Fig. 22(b). It is noticed that temperature of Fig. 22(a) is nearly 42°C whereas for Fig. 22(b) it ranges from 24-28°C. So if some forced air flow can be arranged better heat sinking can be achieved with the same antenna structure. In most commercial applications, a fan is usually used to create air flow over heat sink, and in that case more temperature reduction can be achieved compared to that without any forced air flow depending on fan speed.

VI. BEAMFORMING BOARD LAYOUT, ANTENNA APERTURE, AND EXPERIMENTAL VERIFICATION
A. BFN LAYOUT, RFIC AND 3D METAL PRINTED ANTENNA APERTURE
In Fig. 23, the location of the two RFICs, position of the dual polarized antennas, and the antenna footprint in the BFN board layout is shown. Anokiwave RFICs (AWS-0101) [19]
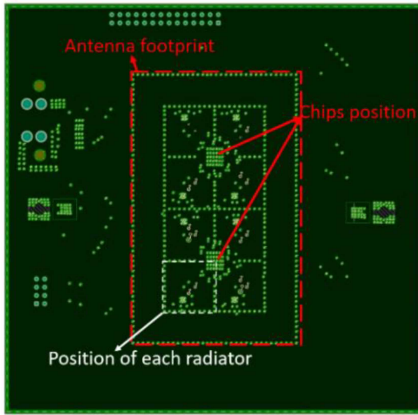
FIGURE 23. The beamforming board layout, showing the position of chips and antenna.

are used for the beamforming network. The AWS-0101 is a highly integrated silicon quad core IC which finds application in radar and phased arrays. Single chip supports four radiating elements, single beam transmit, and dual beam receive and provides all required beam steering controls for 6 bit phase and gain control. The 6 bit phase control implies each step is of value $2\pi/2^6 = 5.625°$. The device provides 20 dB gain during transmit mode, 13 dBm output power during transmit, and 4.0 dB noise figure (NF) during receive. The device features electrostatic discharge (ESD) protection on all pins, operates from a +1.8V supply, and is packaged in a 56 lead 7x7 QFN for easy installation in planar phased array antennas. The chip footprint is approximately 6 mm x 6 mm. The multilayered beamforming board is fabricated and the antenna aperture is assembled with it. Direct Metal Laser Sintering (DMLS) 3D printing process is employed for the fabrication of the antenna aperture using aluminum alloy (*AlSi10Mg*, conductivity 600000 S/m). Fig. 24(a) shows the fabricated antenna prototype in San Diego State University's Antenna and Microwave Laboratory (AML) inside far-field anechoic chamber that supports pattern measurements within 800 MHz to 40 GHz.

B. BEAMFORMING ALGORITHM

During the development of the graphical user interface (GUI) and beamforming algorithm, the mirror feed structure (for realizing low cross-polarization) is taken care of. The mirror ports must be excited with a 180° phase (as shown in Fig. 12(c)) to achieve in phase or broadside radiation. We have employed uniform excitation in our measurements to demonstrate the performance although if only phased array performance is to be evaluated, we can apply non-uniform excitations also. The beamforming algorithm calculates the necessary phase of each of the channel, which is sent to the beamformer chip from the remote computer through the serial peripheral interface (SPI) controller. The current consumption of each chip is 870 mA at 1.8V which accounts to 1.56 Watts, however in our power experiments it drew only

750 mA, hence for our study we used 1.35 Watts throughout the paper, as mentioned earlier.

C. FABRICATION CHALLENGES AND MEASUREMENT RESULTS

The main effort in this work is heat sink investigations and its experimental verification, however we also performed some beam steering measurements. Since a 3D metal printed antenna structure has a rough surface, we observed that there were air gaps in the assembly after adhering the metal structure to the PCB. This was in part due to the uneven surface roughness of the 3D printed part, but also in part due to the difference of thermal coefficient between the board and the metal structure, as 150°C for 60 minutes is the cure temperature of the conducting adhesive employed to adhere the two parts together. Though the exact thermal expansion coefficient of Aluminum alloy is not available from the manufacturer, but the CTE of Aluminum is 25.5 ppm/°C whereas that of copper is 16.7 ppm/°C, hence, fabricating such an array has still some challenges and a better assembly methodology needs to be considered in future. For this reason, we believe that the antenna array elements were not uniformly excited.

Figs. 24(b) and 24(c) show the comparison of the normalized measured and simulated radiation pattern for broadside, 20° scan angle and −45° scan angle for X-polarized array for $\varphi = 0^0$ plane at 11 GHz, respectively. Though we can see almost the same 3 dB beamwidths for the measured and simulated patterns, but we also noticed the presence of a slight dip in the broadside measured pattern as well as presence of sidelobes and high cross-polarized fields in measured broadside pattern. The measured scan pattern for -45° scan angle is in acceptable agreement with the simulated result, whereas for 20° scan angle there is no gain drop in simulated pattern but measured pattern shows nearly 0.7 dB gain drop. The fabrication issues mentioned earlier has caused disagreements between the measured and simulated radiation pattern results as discussed and also discouraged us from performing exhaustive pattern measurements. However, it slightly affected heat sink experimental verification. Fig. 24(d) shows the temperature distribution of the fabricated array measured using an infra-red (IR) camera. We can see the measured maximum temperature of the antenna is nearly 41°C, whereas the maximum temperature distribution ranges from 40-41°C in the simulated result (Fig. 18). So in case of the thermal analysis, measured results are in good agreement with the simulated results. We can also see the temperature of the PCB from backside in Fig. 24(e). In Fig. 24(e), it is seen that each chip is nearly 60°C, which agrees with that observed in Fig. 19(c). Thus, we can infer that the measured heat sink results are in good agreement with the simulated ones.

VII. CONCLUSION

As far as we know, this is the first dual linear polarized all 3D metal printed phased array antenna integrated with
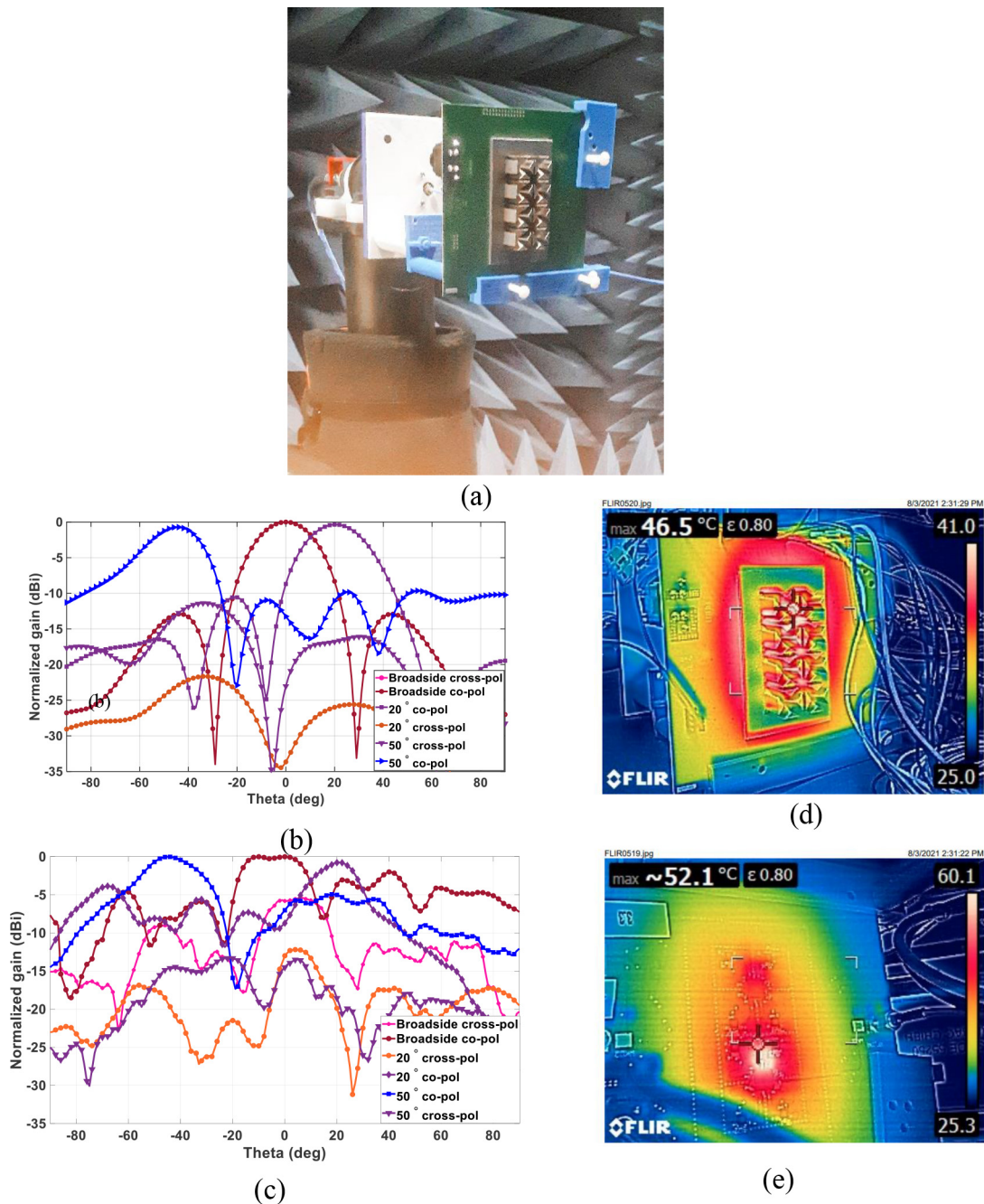
(a)

(b)

(c)

(d)

(e)

FIGURE 24. (a) Fabricated antenna in anechoic chamber, (b) normalized simulated radiation pattern at broadside, 20° scan angle and −45° scan angle for $\varphi = 0^0$ plane at 11 GHz for X-polarized array, (c) normalized measured radiation pattern at broadside, 20° scan angle, and −45° scan angle for $\varphi = 0^0$ plane at 11 GHz for X-polarized array, (d) The temperature distribution of the fabricated antenna array measured by IR camera, and (e) The temperature distribution of the antenna's BFN side (Backside) measured by IR camera.

RFICs based BFN where radiating elements are also serving as heat sink structures. The heat sink study has been validated with an IR camera. The antenna employs Anokiwave chips to generate dual linear polarization as well as achieve beam-steering performances. The mirror feed technique is applied to improve the cross-polarized fields. The antenna covers 8.5 GHz to 11 GHz with acceptable radiation patterns and low cross-polarized fields, and scans till ±50° in both X- and Y-polarizations. The maximum temperature on the

antenna array is only 41°C, which indicates the fact that the antenna aperture is working as an efficient heat sink. We have achieved temperature reduction by 60°C with 4x2 antenna array heat sink structure when compared to temperature distribution of the BFN stack-up without the 4x2 array heat sink radiator. Though we have faced some fabrication challenges and cannot refabricate it again due to lack of funds, the measured patterns and temperature distribution prove that this dual linear polarized all metal antenna is working as heat

sink also. Such an array antenna can be extended to other frequency bands and larger array sizes except that further maturity in fabrication and integration of a metal radiator with BFN board is needed.

ACKNOWLEDGMENT

REFERENCES

[1] C. A. Balanis, *Antenna Theory: Analysis and Design*, 4th ed. Hoboken, NJ, USA: Wiley, Feb. 2016.

[2] R. J. Mailloux, *Phased Array Antenna Handbook*, 2nd ed. Norwood, MA, USA: Artech House, 2005.

[3] J.-C. S. Chieh *et al.*, "Development of flat panel active phased array antennas using 5G silicon RFICs at Ku- and Ka-bands," *IEEE Access*, vol. 8, pp. 192669–192681, 2020.

[4] S. K. Sharma and J.-C. S. Chieh, *Multifunctional Antennas and Arrays for Wireless Communication Systems*. Piscataway, NJ, USA: IEEE Press, May 2021.

[5] G. Mishra, S. K. Sharma, J.-C. S. Chieh, and R. B. Olsen, "Ku-band dual linear-polarized 1-D beam steering antenna using parabolic-cylindrical reflector fed by a phased array antenna," *IEEE Open J. Antennas Propag.*, vol. 1, pp. 57–70, 2020.

[6] C. F. Lee, K. Li, S. Y. Poh, R. T. Shin, and J. A. Kong, "Electromagnetic radiation from a VLSI package and heatsink configuration," in *Proc. IEEE Int. Symp. Electromagn. Compat.*, Jul. 1991, pp. 393–398.

[7] C. E. Brench, "Heatsink radiation as a function of geometry," in *Proc. IEEE Symp. Electromagn. Compat.*, Aug. 1994, pp. 105–109.

[8] P. Qu, M. K. Iyer, and Y. Qiu, "Radiated emission from pin-fin heat sink mounted on an EBGA package," in *Proc. IEEE 8th Top. Meeting Electr. Perform. Electron. Packag.*, 1999, pp. 199–202.

[9] K. Li, C. F. Lee, S. Y. Poh, R. T. Shin, and J. A. Kong, "Application of FDTD method to analysis of electromagnetic radiation from VLSI heatsink configurations," *IEEE Trans. Electromagn. Compat.*, vol. 35, no. 2, pp. 204–214, May 1993.

[10] X. He and T. H. Hubing, "Mitigation of unintentional radiated emissions from tall VLSI heatsinks using ground posts," *IEEE Trans. Electromagn. Compat.*, vol. 55, no. 6, pp. 1271–1276, Dec. 2013.

[11] L. Covert and J. Lin, "Simulation and measurement of a heatsink antenna: A dual-function structure," *IEEE Trans. Antennas Propag.*, vol. 54, no. 4, pp. 1342–1349, Apr. 2006.

[12] J. J. Casanova, J. A. Taylor, and J. Lin, "Design of a 3-D fractal heatsink antenna," *IEEE Antennas Wireless Propag. Lett.*, vol. 9, pp. 1061–1064, Nov. 2010.

[13] S. M. Duffy, G. A. Brigham, K. B. Newman, and J. S. Herd, "Stepped notch antenna array used as a low thermal resistance heat sink," in *Proc. IEEE Antennas Propag. Soc. Int. Symp. (APSURSI)*, 2013, pp. 622–623.

[14] J. Qian, M. Tang, Y.-P. Zhang, and J. Mao, "Heatsink antenna array for millimeter-wave applications," *IEEE Trans. Antennas Propag.*, vol. 68, no. 11, pp. 7664–7669, Nov. 2020.

[15] R. Banerjee, S. K. Sharma, P. Nguyen, J.-C. S. Chieh, and R. Olsen, "Investigations of all metal heat sink dual linear polarized phased array antenna for ku-band applications," in *Proc. Int. Appl. Comput. Electromagn. Soc. Symp. (ACES)*, 2020.

[16] "Ansys Icepak Help." [Online]. Available: https://www.ansys.com (Accessed: Dec. 10, 2021).

[17] "rogerscorp.com." [Online]. Available: https://rogerscorp.com/advanced-electronics-solutions//ro4000-series-laminates/ro4350b-laminates (Accessed: Dec. 10, 2021).

[18] K. Woelder and J. Granholm, "Cross-polarization and sidelobe suppression in dual linear polarization antenna arrays," *IEEE Trans. Antennas Propag.*, vol. 45, no. 12, pp. 1727–1740, Dec. 1997.

[19] "anokiwave.com." [Online]. Available: https://www.anokiwave.com/products/aws-0101/index.html (Accessed: Dec. 10, 2021).

RUDRAISHWARYA BANERJEE (Student Member, IEEE) received the B.Tech. and M.Tech. degrees (with specialization in microwave and wireless engineering) in radio physics and electronics from the University of Calcutta in 2013 and 2015, respectively. She is currently pursuing the Ph.D. degree with the San Diego State University, San Diego, CA, USA, and the University of California at Irvine, Irvine, CA, USA, under a joint doctoral program.

Her research interest includes different types of dual linear/circular polarized RFIC-based phased array antennas with integrated beamforming network for SATCOM applications. She serves as a Reviewer for IEEE ANTENNAS AND WIRELESS PROPAGATION LETTERS.

SATISH KUMAR SHARMA (Senior Member, IEEE) received the B.Tech. degree in electronics engineering from the Kamla Nehru Institute of Technology and the Ph.D. degree in electronics engineering from the Indian Institute of Technology, Banaras Hindu University in 1991 and 1997, respectively.

From March 1999 to April 2001, he was a Postdoctoral Fellow with the Department of Electrical and Computer Engineering, University of Manitoba, Winnipeg, MB, Canada. He was a Senior Antenna Engineer with InfoMagnetics Technologies Corporation, Winnipeg, from May 2001 to August 2006. Simultaneously, he was also a Research Associate with the University of Manitoba from June 2001 to August 2006. In August 2006, he joined San Diego State University, San Diego, as an Assistant Professor with the Department of Electrical and Computer Engineering. Here, he has developed an Antenna Laboratory, teaches courses in Applied Electromagnetics, and advises B.S., M.S. & Ph.D. students and a Postdoctoral Fellows. Since 2014, he has been a Full Professor and the Director of the Antenna and Microwave Laboratory. He is author/coauthored more than 285 research papers published in the referenced international journals and conferences. He has co-edited three volumes of *Handbook of Reflector Antennas and Feed Systems, Volume 1: Theory and Design of Reflectors, Volume II: Feed Systems, and Volume III: Applications of Reflectors* (Artech House, USA). His new coedited/coauthored book is *Multifunctional Antennas and Arrays for Wireless Communication Systems* (IEEE Press/Wiley, USA). His main research interests are in the millimeter wave antennas, beam steering antennas, massive MIMO antennas, 5G communication antennas, beamforming networks, antennas for IoT, miniaturized antennas, ultra-wideband, multiband and broadband antennas, reconfigurable and frequency agile antennas, feeds for reflector antennas, waveguide horns and polarizers, electrically small antennas, RFID antennas, active antennas, frequency selective surfaces, metasurfaces, and microwave passive components.

Dr. Sharma received the IEEE AP-S Harold A. Wheeler Prize Paper Award in 2015, the National Science Foundation's Prestigious Faculty Early Development (CAREER) Award in 2009, the Young Scientist Award of URSI Commission B, Field and Waves, during the URSI Triennial International Symposium on Electromagnetic Theory, Pisa, Italy, in 2004. He was recognized as the Outstanding Associate Editor (AE) for the IEEE TRANSACTION ON ANTENNAS AND PROPAGATION in July 2014. He served as the AE for the IEEE TRANSACTION ON ANTENNAS AND PROPAGATION and currently serving as the AE for the IEEE ANTENNAS AND WIRELESS PROPAGATION LETTERS. He was the Chair/Co-Chair of the several Student Paper Contests in different conferences and symposia and served on the sub-committee of the Education Committee for the IEEE Antennas and Propagation Society for the organization of the Student Paper Contests. He is a Full Member of the USNC/URSI, Commission B, Senior Member of URSI and currently serving as Chair, Technical Activities for the USNC/URSI Commission B.

JIA-CHI SAMUEL CHIEH (Senior Member, IEEE) received the B.S. degree in electrical engineering from the University of California at San Diego, La Jolla, CA, USA, in 2004, the M.S. degree in electrical engineering from the University of Southern California, Los Angeles, CA, USA, in 2007, and the Ph.D. degree in electrical engineering from the University of California Davis at Davis, Davis, CA, USA, in 2012. In Summer 2009, he was a Student Intern with PlanarMag Inc., aiding in the development and design of magnetic baluns for TV set-top boxes. In Summer 2010, he was a Student Intern with LGS Innovations (formerly, Bell Laboratories), Florham Park, NJ, USA, aiding in the development and modeling of millimeter-wave antennas, arrays, and flip-chip packages. In 2012, he joined the Naval Information Warfare Center Pacific (NIWC-PAC) in San Diego and his current interests include developing microwave and millimeter-wave phased arrays for directional networking as well as novel antennas for nanosatellite applications. He has designed over 6 RFIC-based phased array antennas from C- thru W-Bands. He is currently the RF lead for the Integrated Circuits Technology branch at NIWC-PAC. He has been a Principle Investigator of three ONR funded S&T projects at the 6.2 level. He has also been serving as an Adjunct Lecturer with the University of San Diego since 2013 and an Adjunct Faculty with San Diego State University since 2018.

RAIF FARKOUH received the B.S. and M.S. degrees in electrical engineering from the University of Nebraska–Lincoln in 2017. His specialty was microelectronics. He has worked as an electrical engineering intern with Nebraska Public Power District, where he worked on the design and specification of power and control systems, system layouts, load calculations, equipment sizing and selection. In addition, he worked as an electrical engineering intern with Jensen Hughes Consulting Company, where he performed circuit analysis and supporting tasks to support safe-shutdown analysis of a nuclear power station. He also worked as a Research Assistant with the University of Nebraska–Lincoln, where he developed and carried out research projects to demonstrate capability of Femtosecond Laser Machining. In 2018, he joined Naval Information Warfare Center Pacific, San Diego, CA, USA, as an Electrical Engineer. He is the primary investigator for a project with the goal to develop wideband low-cost electronically scanned Ka-band circular polarized antenna array technology to provide DoD ground and space-based systems with electronically steerable high level system arrays capable of supporting LEO small satellite constellations. He has designed several phased array antennas in the X, Ku, and Ka-bands. He also supported the testing and evaluation of novel RF Integrated Circuits including amplifiers, filters, and antenna array chipsets.